*Rev. Mexicana Astron. Astrof.*, **24**, 27-42 (1992)

# IRRADIATION OF ACCRETION DISKS AROUND YOUNG OBJECTS. II. CONTINUUM ENERGY DISTRIBUTION

Nuria Calvet[1,2], Gladis Magris C.[1], Alberto Patiño[1,3], and Paola D'Alessio[1,4]

*Received 1991 June 5*

RESUMEN

Hemos calculado el flujo emergente de sistemas compuestos de una estrella jóven rodeada de un disco de acrecimiento físicamente delgado, ópticamente grueso, sujeto a irradiación por la estrella. Hemos encontrado lo siguiente: (1) el continuo emergente es más bajo que el calculado con la suposición que toda la energía se deposita en el fondo de la atmósfera en cada anillo; por lo tanto, los discos deben abrirse más o tener tasas de acrecimiento de masa más altas de lo que se pensaba anteriormente; (2) la irradiación domina a grandes radios en el disco, produciendo una inversión de temperatura en la atmósfera del mismo. El radio en el disco donde la irradiación se hace más importante que el calentamiento viscoso aumenta cuando la tasa de acrecimiento aumenta o la temperatura efectiva de la estrella disminuye; (3) la intensidad en absorción de las bandas de CO, $H_2O$, TiO y de silicato en 10 $\mu$m es una medida de la tasa de acrecimiento de masa; (4) los discos de acrecimiento ópticamente gruesos pueden reproducir $\sim$ 40% de los colores infrarrojos cercanos de estrellas T Tauri. Los discos con grandes pendientes y grandes tamaños, $R_{max} \leq 100$ UA, pueden explicar el exceso infrarrojo lejano, pero todavía no pueden explicarse los colores de $\approx$ 20% de los objetos; (5) este estudio sugiere que los parámetros del disco pueden determinarse a partir de los siguientes observables: $\dot{M}$ puede ser determinado a partir de las bandas moleculares de $H_2O$, CO y TiO; la pendiente del disco por el silicato, si se conoce $\dot{M}$; con éstas, el radio máximo del disco puede determinarse a partir del flujo a $\lambda > 10\mu$m. Se requiere espectrofotometría infrarroja de alta resolución para probar estas predicciones.

ABSTRACT

We have calculated the emergent flux for systems composed of a young star and a steady, infinitely thin, optically thick accretion disk subject to irradiation from the central star. We have found the following: (1) the emergent continuum flux is lower than that calculated assuming that all the stellar energy is deposited at the bottom of the atmosphere at each annulus of the disk; thus, disks must have larger flaring, or larger accretion rates than previously thought; (2) irradiation determines the heating at large radii, producing a temperature inversion in the disk atmosphere. The disk radius where the heating due to irradiation becomes more important than viscous heating increases when the mass accretion rate increases and when the stellar effective temperature decreases; (3) the absorption strength of the CO, $H_2O$, TiO bands, and of the 10$\mu$m silicate feature is a measure of the mass accretion rate $\dot{M}$; (4) optically thick accretion disks can reproduce $\sim$ 40% of the near-infrared color observations for T Tauri stars. Large degrees of flaring and large disk sizes, $R_{max} \leq 100$ AU, can explain objects with fairly large far-infrared excess, but still $\approx$ 20% of the objects cannot be understood with the present models; (5) this study suggests that disk parameters can be determined with the following observables: $\dot{M}$ can be determined from the molecular bands of $H_2O$, CO, and TiO; the flaring of the disk can be determined from the silicate feature, once $\dot{M}$ is known; and with these, the maximum radius of the disk can be determined from the flux at $\lambda > 10$ $\mu$m. High resolution infrared spectrophotometric data are required to test these predictions.

*Key words:* **ACCRETION DISKS – INFRARED SOURCES – STARS-FORMATION**

1. Centro de Investigaciones de Astronomía, Venezuela.
2. Also Grup d'Astrofisica de la Societat Catalana de Fisica (Institut d'Estudis Catalans).
3. Universidad de Los Andes, Venezuela.
4. Instituto de Astronomía, UNAM, México.

## I. INTRODUCTION

In a previous paper (Calvet *et al.* 1991, hereafter Paper I), we have calculated the structure of the atmospheres of accretion disks around young objects, subject to irradiation of light from the central star. The flux in the near-infrared CO bands emerging from the star plus a disk system was calculated with these model atmospheres and it was shown that the strength of the CO band was a good indicator of the mass accretion rate. In this paper, we calculate the continuum energy distribution from 0.5$\mu$m to 100$\mu$m for the system, for values of parameters characterizing the central object and the steady disk appropriate to young objects. Accretion disks around young objects have mostly been discussed in the literature in the context of T Tauri stars (hereafter TTS). However, the large infrared excess observed in Herbig's Ae and Be stars with luminosities larger than $\sim$1.5 times the stellar luminosity could also be interpreted in terms of accretion luminosity from disks with an average mass accretion rate of $5 \times 10^{-6}$ $M_\odot$ $yr^{-1}$ (Strom *et al.* 1990). Therefore, in this paper we present model disks appropriate to TTS and to Herbig's Ae and Be stars.

Reprocessing of stellar light by the disk atmosphere in a flared disk produces spectral energy distributions flatter than the standard $\lambda F_\lambda \propto \lambda^{-4/3}$ characteristic of flat accretion disks, and in much better agreement with observations of TTS (Kenyon and Hartmann 1987, hereafter KH). So far, the continuum from T Tauri disks has been calculated assuming that all the stellar light arrives at the atmospheric depth where the continuum forms (KH; Adams, Lada, and Shu 1987; Bertout, Basri, and Bouvier 1988). However, as shown in Paper I, part of the stellar energy is deposited in the upper atmospheric layers, and the effective temperature in the disk is lower than that estimated so far. We compare the resultant energy distributions calculated under both assumptions and find that for low mass accretion rates fluxes are lower than those calculated with the direct reprocessing hypothesis.

Since no calculations of disk model atmospheres in young objects have been presented preceding this paper and Paper I, no detailed spectrum calculations have been shown either. The need for these calculations has not been urgent, however, because few high resolution infrared observations exist. This situation may change in the near future, so it becomes pertinent now to present detailed spectra. We find that conspicuous features appear in the 0.7 to 10 $\mu$m range: the TiO, $H_2O$, and CO molecular bands, and the silicate dust feature, which we find to be indicators of the mass accretion rate and the flaring of the disk. The flux beyond 10 $\mu$m, on the other hand, for known values of the mass accretion rate and the flaring of the disk, depends on the assumed maximum radius. Taken together, these observable quantities can give estimates of the relevant disk parameters, in the standard disk model we are assuming.

In §II, we describe the method of calculation and the different assumptions used. In §III, we present the results and in §IV, we discuss the implications of those results. Finally, we give a summary in §V.

## II. CALCULATIONS

The method of calculation of the disk temperature structure is discussed in detail in Paper I so it is only outlined here. We consider a viscous, geometrically thin, optically thick, flared and steady accretion disk, of minimum radius $R_{min}$ and maximum radius $R_{max}$, with constant mass accretion rate $\dot{M}$ around a star with mass $M_*$ and radius $R_*$. The disk height $H$ is assumed to vary with distance to the star $r$ as $H = H_0(r/R_*)^\gamma$, where we take $H_0 = 0.1\ R_*$. We neglect viscous dissipation in the disk atmosphere so radiative equilibrium holds. The incident radiation is considered as a parallel beam with $E_0$ energy per unit area incident at an angle $\cos^{-1}\mu_0$ from the normal to the atmosphere boundary. A fraction $\alpha$ of this energy is absorbed in the atmosphere and a fraction $\sigma = 1 - \alpha$ is scattered. The temperature in the atmosphere is determined by the viscous energy generation in the interior of the disk and by the stellar flux absorbed as it travels down the atmosphere. We follow the approximate treatment of Milne (1930) and Strittmatter (1971) to calculate the temperature structure in the disk, for which we obtain (Paper I)

$$T^4(\tau_d) = \frac{3}{4}T_v{}^4(\tau_d + \frac{2}{3}) + \\ + \frac{\alpha E_0 \mu_0}{4\sigma_R}[C_1' + C_2' e^{-q\tau_d/\mu_0} + C_3' e^{-\beta q \tau_d}] \ , \qquad (1)$$

where

$$C_1' = (1 + C_1)(2 + \frac{3\mu_0}{q}) + C_2(2 + \frac{3}{\beta q})$$

$$C_2' = \frac{(1 + C_1)}{\mu_0}(q - \frac{3\mu_0{}^2}{q})$$

$$C_3' = C_2\beta(q - \frac{3}{q\beta^2})$$

and

$$C_1 = -\frac{3\sigma\mu_0{}^2}{1 - \beta^2\mu_0{}^2}$$

$$C_2 = \frac{\sigma(2 + 3\mu_0)}{\beta(1 + \frac{2\beta}{3})(1 - \beta^2\mu_0{}^2)}$$

Here, $\tau_d$ is the optical depth in the disk, calculated with the Rosseland mean opacity, $\beta = (3\alpha)^{1/2}$, and $q$ is the ratio of the opacity in the wavelength range where the stellar radiation is absorbed to that in the range where the atmospheric gas emits. The opacity in each of these wavelength ranges is calculated as a mean over the interval of the inverse of the monochromatic opacity weighted by the derivative of the Planck function relative to the temperature (so the opacity in the second wavelength range corresponds to the Rosseland mean opacity). The treatment of Milne (1930) and Strittmatter (1971) assumes that the atmosphere is grey, and that $q$ and $\alpha$ are constant throughout the atmosphere. We adopt in the application of equation (1) to the disk atmosphere values of $q$ and $\alpha$ evaluated at the temperature and pressure of the surface (Paper I). The treatment also assumes that the two wavelength ranges are clearly separated, so there is no atmospheric emission in the first range nor scattered stellar radiation in the second. This hypothesis is not appropriate for the inner regions of disks around young stellar objects, but we adopt it given the exploratory nature of this work. It becomes more appropriate in the outer regions, where $T \leq 1500$ K and dust opacity dominates.

The temperature $T_v$ in equation (1) is the "viscous temperature", that is, the temperature for a disk in which accretion is the dominant energy source. It is given by

$$T_v = \left[\frac{3GM_*\dot{M}}{4\pi\sigma_R r^3}\left(1-\left(\frac{R_*}{r}\right)^{1/2}\right)\right]^{1/4}. \quad (2)$$

(Shakura and Sunyaev 1973). The Eddington approximation has been adopted to obtain equation (1).

To calculate the structure of the atmosphere at each radius $r$ in the disk, once the temperature structure is calculated with equation (1), we assume that the height of the disk $H$ corresponds to the level $\tau = 2/3$, and solve by iteration the system of equations for the pressure and height

$$dp/d\tau = g(z)/\chi_{Ross}, \quad (3)$$

and

$$dz/d\tau = -1/\chi_{Ross}\rho, \quad (4)$$

where the height-dependent gravity is given by

$$g(z) = \frac{GM_*H}{r^3}\frac{(1+z/H)}{[1+(z+H)^2/r^2]^{3/2}}. \quad (5)$$

In these equations, $\chi_{Ross}$ is the Rosseland mean opacity, $\rho$ is the density, and $z$ is the height of the atmosphere above the $\tau = 2/3$ level. Atomic and molecular populations are calculated assuming LTE. The assumption that the disk is optically thick is checked *a posteriori* by calculating the mass column density of the atmosphere at large optical depth and comparing it to the total mass column density of a steady disk, $\Sigma = (\dot{M}/\alpha_v c_s H)(1-(R_*/r)^{1/2})$, where $\alpha_v$ is the disk $\alpha$ parameter (Shakura and Sunyaev 1973). We find that the mass column density of the atmosphere is smaller than $\Sigma$ if $\alpha_v$ is of the order of $10^{-2}$ to $10^{-3}$. These values are appropriate for describing the characteristic of disks in FU Orionis objects (Clarke, Lin, and Pringle 1990), which are considered to be disks around TTS where an instability is taking place (Hartmann and Kenyon 1985), and could be appropriate to those disks in other phases.

The Rosseland mean opacity and monochromatic fluxes have been calculated assuming LTE with opacity constituents listed in Paper I. The Rosseland mean opacity calculated here agrees with that of Alexander, Johnson, and Rypma (1983), but is higher than that in Alexander, Augason, and Johnson (1989), who use an opacity-sampled treatment for the water opacity. The most important features due to gas opacity in the calculated spectra are the TiO bands in the optical, and the water bands and the CO bands in the infrared. We use the harmonic-mean opacity of water vapor of Auman (1967), which agrees well with the laboratory data of Ludwig *et al.* (1973) for $\lambda < 3.5$ $\mu$m, but is too weak at larger wavelengths. The pure rotational band is from Tsuji (1966). The opacity in the near-infrared CO bands is calculated using wavelengths from Mantz *et al.* (1975) and oscillator strengths from Kirby-Docken and Liu (1978). A Doppler profile is assumed for the lines. The opacity for the $\alpha$, $\gamma$ and $\phi$ systems of TiO is taken from Collins and Fay (1974), with electronic oscillator strengths from Davis *et al.* (1986). The microturbulent velocity has been taken equal to the local sound speed. Other important spectral features are due to dust. We use the dust grain size distribution as in Draine and Lee (1984), with grain properties from Draine (1987), with abundances appropriate for the interstellar medium. We assume that grains are destroyed above 1500 K.

To calculate the emergent flux, the disk is divided into annuli. At each annulus, an atmospheric calculation is preformed and monochromatic intensities are obtained for several inclination angles. LTE is assumed for the source functions. The flux of the system is obtained adding the stellar intensity to the the intensities of the annuli, weighted by their projected surface areas. The individual intensities have

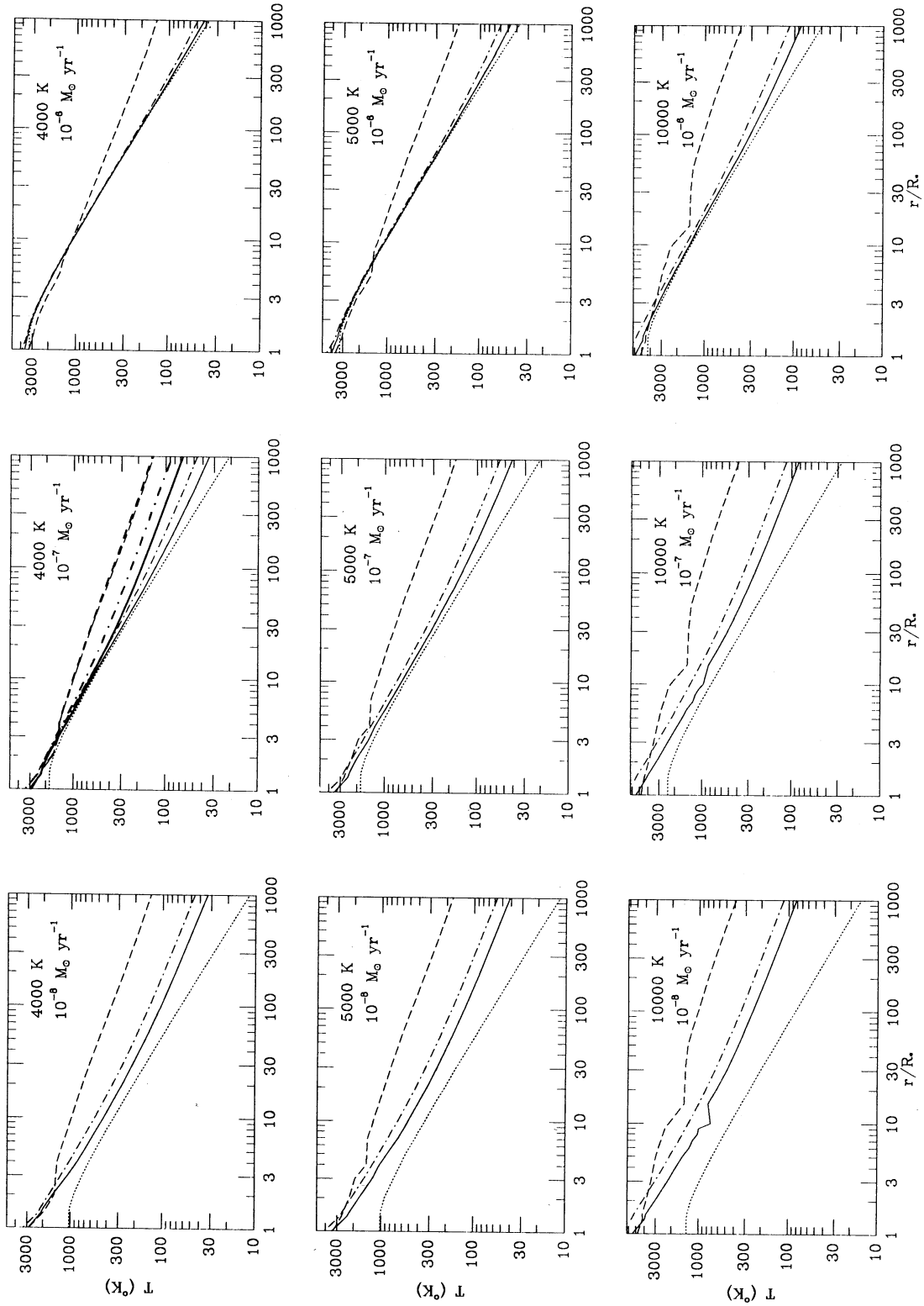


Fig. 1. Characteristic temperatures for disk atmospheres for models with stellar effective temperature and mass accretion rate specified on each plot: the temperature at $\tau_d = 2/3$, $T_{eff}$ (continuous line); the effective temperature the disk would have if there was no irradiation, $T_v$ (dotted line); the temperature of the atmosphere at $\tau_d = 2/3$ if all the stellar energy were deposited at that level, $T_{rep}$ (dot-dash line); the surface temperature, $T_0$ (dashed line). Models shown in light lines have $\gamma = 9/8$ and $R_{max} = 1000\ R_*$. Model with $T_* = 4000$ K, $\dot{M} = 10^{-7}$ M$_\odot$ yr$^{-1}$ $R_{max} = 1000\ R_*$ and $\gamma = 5/4$ is shown in heavy lines (see text).

TABLE 1

CALCULATED MODELS

| Num. | $M_*$ ($M_\odot$) | $R_*$ ($R_\odot$) | $T_*$ (K) | $\dot{M}$ ($M_\odot$ yr$^{-1}$) | $R_{min}$ ($R_*$) | $R_{max}$ ($R_*$) | $\gamma$ |
|---|---|---|---|---|---|---|---|
| 1 | 1 | 3 | 4000 | $10^{-8}$ | 1 | 1000 | 9/8 |
| 2 | 1 | 3 | 4000 | $10^{-8}$ | 1 | 8000 | 9/8 |
| 3 | 1 | 3 | 4000 | $10^{-8}$ | 1 | 1000 | 5/4 |
| 4 | 1 | 3 | 4000 | $10^{-8}$ | 1 | 8000 | 5/4 |
| 5 | 1 | 3 | 4000 | $10^{-7}$ | 1 | 1000 | 9/8 |
| 6 | 1 | 3 | 4000 | $10^{-7}$ | 1 | 8000 | 9/8 |
| 7 | 1 | 3 | 4000 | $10^{-7}$ | 1 | 1000 | 5/4 |
| 8 | 1 | 3 | 4000 | $10^{-7}$ | 2 | 1000 | 5/4 |
| 9 | 1 | 3 | 4000 | $10^{-7}$ | 3 | 1000 | 5/4 |
| 10 | 1 | 3 | 4000 | $10^{-7}$ | 1 | 8000 | 5/4 |
| 11 | 1 | 3 | 4000 | $10^{-6}$ | 1 | 1000 | 9/8 |
| 12 | 1 | 3 | 5000 | $10^{-8}$ | 1 | 1000 | 9/8 |
| 13 | 1 | 3 | 5000 | $10^{-7}$ | 1 | 1000 | 9/8 |
| 14 | 1 | 3 | 5000 | $10^{-6}$ | 1 | 1000 | 9/8 |
| 15 | 3 | 3 | 10000 | $10^{-8}$ | 1 | 1000 | 9/8 |
| 16 | 3 | 3 | 10000 | $10^{-7}$ | 1 | 1000 | 9/8 |
| 17 | 3 | 3 | 10000 | $10^{-6}$ | 1 | 1000 | 9/8 |
| 18 | 3 | 3 | 10000 | $10^{-5}$ | 1 | 1000 | 9/8 |

not been rotationally broadened. This is not important for the broad spectral features, but results in fictitiously strong bands of CO at high inclinations. The fundamental CO bands have not been calculated. The photospheric fluxes were calculated from model atmospheres in Carbon and Gingerich (1969), adopting log g = 4.

## III. RESULTS

### a) *Atmospheric Temperature*

We have calculated the spectral flux distribution for models with characteristics specified in Table 1. We assumed that the viscous temperature between 1 and 1.36 $R_*$ was the same as in $r = 1.36\ R_*$.

Figure 1 shows the effective temperature $T_{eff}$, i.e., the temperature at $\tau_d = 2/3$, and the surface temperature $T_0$ as a function of distance to the star for models with different $\dot{M}$ and $T_*$, and $\gamma = 9/8$, $R_{max} = 1000\ R_*$ in Table 1. The characteristic temperatures shown in Figure 1 are different from those calculated for the same models in Paper I. This is due to the fact that the TiO opacity was improved in the present calculation, changing the values of the parameter $q$. The viscous temperature $T_v$ given by equation (2), that is, the effective temperature that the disk atmosphere would have in the case of no irradiation, is also shown for comparison. As discussed in Paper I, the implicit equation that is solved at low optical depth to obtain the values of $T_0$, $q$, and $\alpha$, for given $E_0$, $\mu_0$, and surface pressure, has a discontinuity produced by the adopted abrupt jump in opacity at 1500 K, where we assume that dust sets in. This results in jumps in the values of the characteristic temperatures apparent in Figure 1.

Irradiation controls the temperature structure in the atmosphere in the case of low mass accretion rates; only when the mass accretion rate becomes $\geq 10^{-6}\ M_\odot\ yr^{-1}$, the temperature at the level where the continuum forms is determined mainly by the viscous flux coming from inside the disk. However, as discussed in Paper I (see also KH), the effect of irradiation increases with distance to the star for a non-flat disk, so that even in the cases with high $\dot{M}$ shown in Figure 1, $T_{eff} > T_v$ at large radii.

Figure 1 also shows the "reprocessing temperature",

$$T_{rep} = (T_v^4 + E_0\mu_0/\sigma_R)^{1/4}, \qquad (6)$$

which is the temperature of the atmosphere at the level $\tau_d = 2/3$ if all the stellar energy were deposited at that level. It can be obtained from equation (1) in the case that $q \sim 0$ and $\alpha = 1$. However, since there is energy deposition at the upper levels, the reprocessing temperature is always higher than the effective temperature, and they begin to be similar to each other (and to $T_v$) at high mass accretion rates.

The stellar flux absorbed in the outermost atmospheric layers raises the temperature of those layers relative to the viscous case, and can even produce a temperature inversion. It can be shown that for the case in which the viscous terms can be neglected in equation (1), $T_0/T_{eff} \sim (q/4\mu_0)^{1/4}$ (Paper I). Since $\mu_0 < 1$ and $q \geq 1$, there is a temperature inversion whenever irradiation dominates. As $r$ increases, $\mu_0$ decreases and $q$ increases, so that an increasing fraction of the energy is deposited in the outermost layers and $T_0/T_{eff}$ increases, as shown in Figure 1.

The characteristic temperatures for the case $T_*$ = 4000 K, $\dot{M} = 10^{-7}\ M_\odot\ yr^{-1}$, $R_{max} = 1000\ R_*$ and $\gamma = 5/4$ are also shown in Figure 1, in comparison with the corresponding case for $\gamma$ = 9/8. The reprocessing temperature and the effective temperature increase, but the surface temperature is almost the same. The reason for it is that the incidence angle decreases when the flaring of the disk increases, so $\mu_0$ increases. The level of the atmosphere where the optical depth is of order 1 for the stellar radiation is given by $\tau_d \sim \mu_0/q$; thus as the disk becomes more flared, stellar energy is deposited in deeper layers. This result may also be seen in equation (1). The surface temperature is approximately given by

$$T(0)^4 \sim 1/2T_v^4 + \alpha E_0\mu_0 C_2'/4\sigma_R \sim 1/2T_v^4 + \alpha E_0 q/4\sigma_R,$$

since for the values of the problem $C_2' > C_3' > C_1'$, and $C_2' \sim q/\mu_0$, $\mu_0 < 1$. The value of $T(0)$ is then approximately constant for given $E_0$, $q$ and $\alpha$. On the other hand,

$$T(2/3)^4 \sim T_v^4 + \alpha E_0 \mu_0 C_1'/4\,\sigma_R,$$

since the exponential terms in equation (1) are small. Since $C_1'$ increases slowly with $\mu_0$, the irradiation term increases when $\mu_0$ increases.

b) *Infrared Spectral Energy Distribution*

The emergent flux for the models with $\gamma = 9/8$ and $R_{max} = 1000\ R_*$ at zero inclination is shown in Figure 2, for stellar effective temperatures $T_* = 4000$ K (Figure 2a), $T_* = 5000$ K (Figure 2b), and $T_* = 10000$ K (Figure 2c), and different mass accretion rates. The photospheric flux and the flux of a purely viscous disk with the corresponding accretion rate is also shown for comparison.

In all cases, the irradiated disk dominates the flux at $\lambda > 1$ $\mu$m, and as stated by KH, the flux greatly exceeds that of a purely viscous flux at low mass accretion rates. As $\dot{M}$ increases the effect of irradiation becomes less important. Several spectral features are conspicuous in the spectra shown in Figure 2: the CO first overtone bands 2.3 $\mu$m (the fundamental band at 4.6 $\mu$m was not calculated), the water vapor bands at 1.14, 1.38, 1.87, 2.7, and 6.3 $\mu$m, the TiO bands in the optical, and the silicate feature at 10 $\mu$m. These features are marked for the case $T_* = 4000$ K and $\dot{M} = 10^{-6}$ $M_\odot$ yr$^{-1}$. They follow the behavior already found for the first overtone bands of CO in Paper I: for a given stellar effective temperature, the feature is weakly in absorption, absent, or in emission at low mass accretion rates; as the mass accretion rate increases the feature become stronger in absorption. When the stellar effective temperature increases, the mass accretion rate at which the feature turns from emission to absorption increases. These strong features are formed at low optical depth in the atmosphere and reflect the temperature of the layers affected the most by irradiation. As discussed in the previous section, if heating by irradiation dominates at a given annulus in the disk, there is a temperature inversion in the atmosphere and strong features will be in emission. On the other hand, if viscous heating is

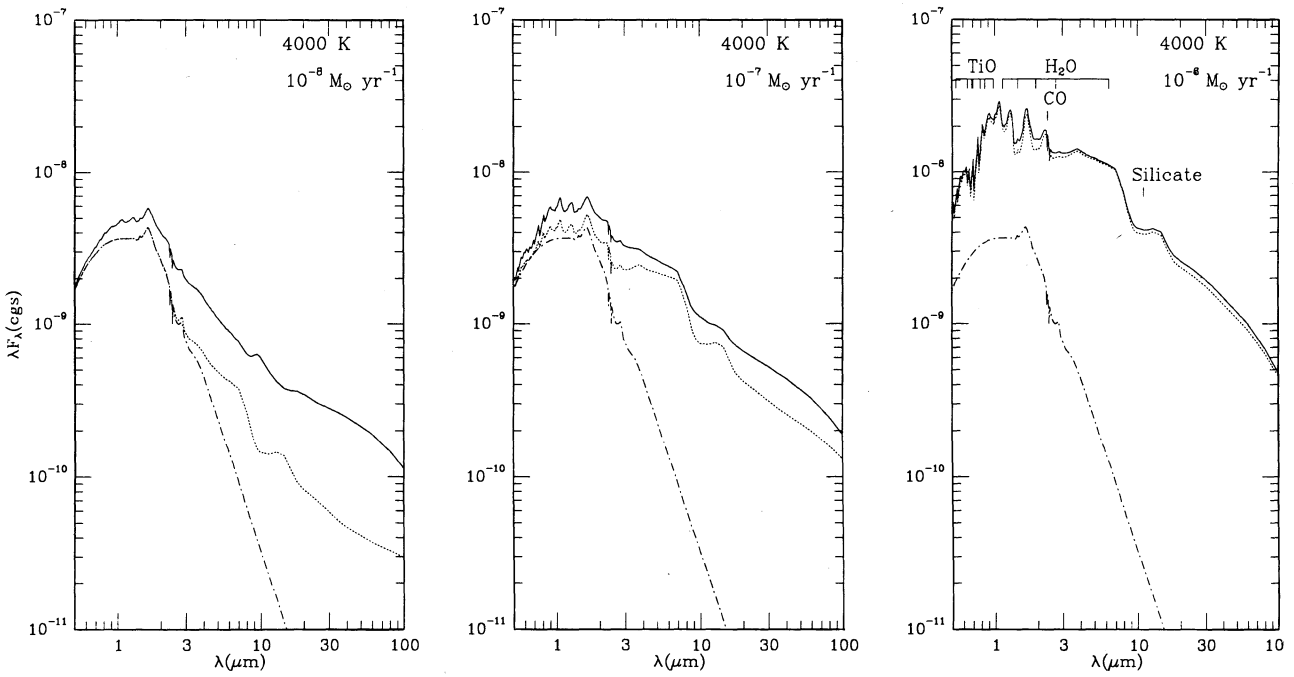


Fig. 2a. Emergent flux for star plus disk systems. $T_* = 4000$ K. The stellar temperature and the mass accretion rate are specified on each plot. Models shown are calculated with $\gamma = 9/8$ and $R_{max} = 1000\ R_*$. Continuous line: composite spectrum, dotted line: viscous disk, dot-dash line: photosphere. Features discussed in the text have been marked for the case $T_* = 4000$ K and $\dot{M} = 10^{-6}$ $M_\odot$ yr$^{-1}$. Fluxes are calculated at 100 pc.

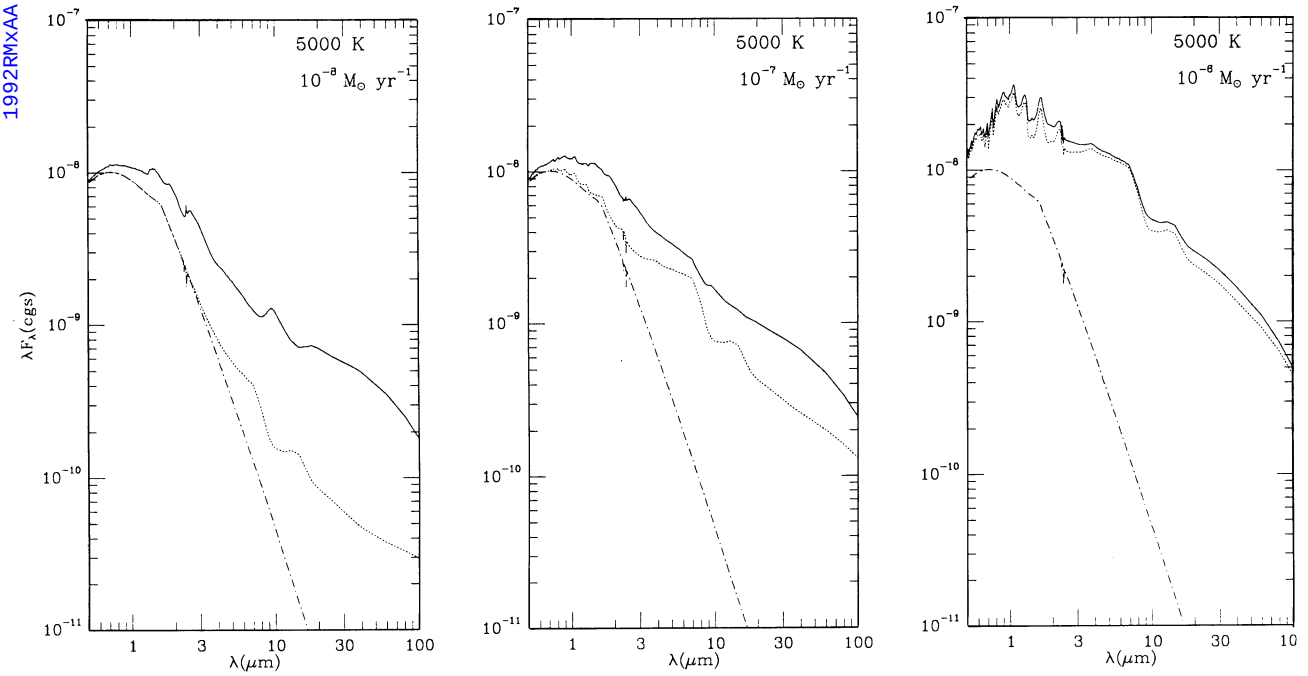


Fig. 2b. Same as Figure 2a for $T_* = 5000$ K.

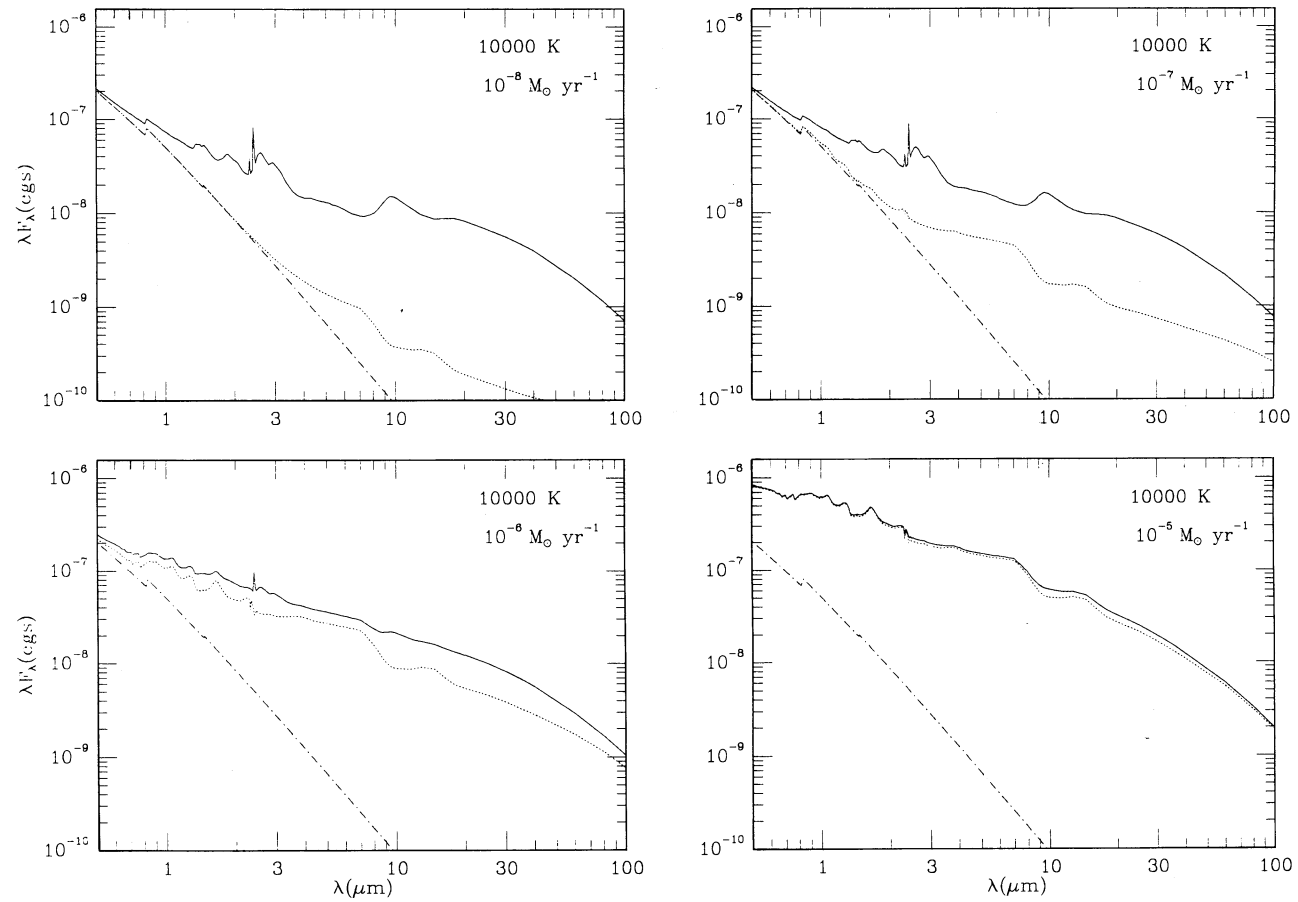


Fig. 2c. Same as Figure 2a for $T_* = 10\,000$ K.

dominant, $T_0/T_{eff} < 1$ and the feature will be in absorption. At low mass accretion rate, irradiation dominates at most disk radii and features in the disk spectrum are in emission. They may appear in absorption in the star+disk spectrum, because the disk emission may not be enough to obliterate the photospheric absorption. In this case, the photospheric feature would appear veiled. As $\dot{M}$ increases, for a given $T_*$, the radius in the disk where irradiation becomes more important than viscous heating increases; a larger region in the disk has $T_0/T_{eff} < 1$, and the feature will be in absorption in the disk spectrum. For a fixed $\dot{M}$, as $T_*$ increases, the zone in the disk where irradiation dominates becomes larger; therefore, higher stellar effective temperatures require higher values of $\dot{M}$ to have the feature in absorption in the star+disk spectrum.

To see the formation of the different features and the sensitivity to the different assumptions, we will study in more detail the reference models characterized by $T_* = 4000$ K and $\dot{M} = 10^{-8}$ and $10^{-7}$ $M_\odot$ $yr^{-1}$, which would be appropriate to most TTS. Figure 3 shows monochromatic intensities for selected annuli in these two models. Molecular features of TiO and $H_2O$ form in annuli with $r \leq 3\ R_*$ while dust opacity dominates for larger radii. When the mass loss rate increases, the effective temperature at inner radii increases (c.f. Figure 1), annular intensities increase, and molecular features become stronger, becoming more conspicuous in the composite star plus disk spectrum (c.f. Figure 2a). However, for radii > 50 $R_*$, annular intensities are comparable, because at those radii irradiation dominates. Hence, the flux of the composite spectrum for $\lambda < 10\ \mu$m is very sensitive to $\dot{M}$, while

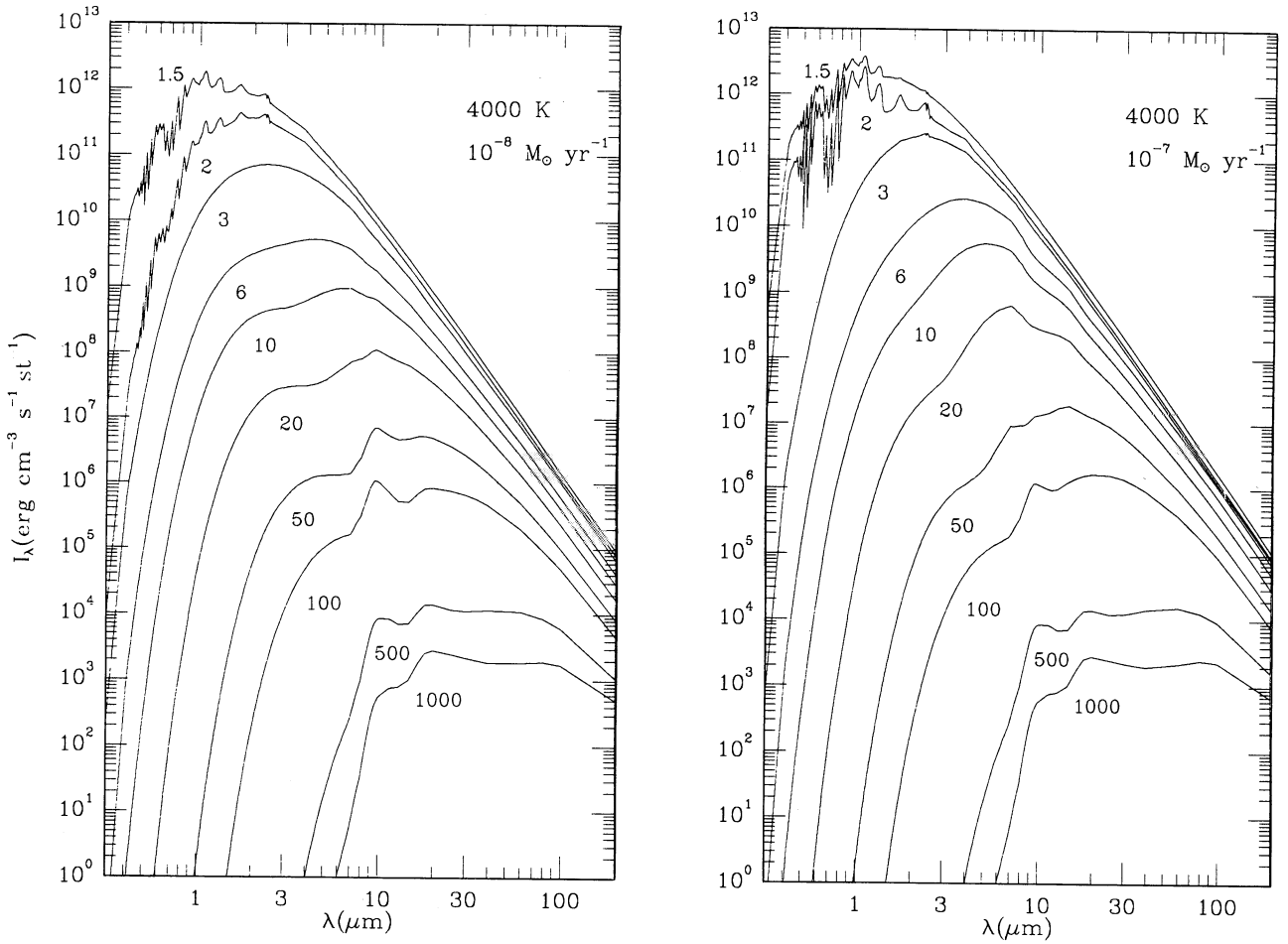


Fig.3. Monochromatic intensities from selected annuli of models with $T_* = 4000$ K, $\gamma = 9/8$, and $R_{max} = 1000\ R_*$. (a) $\dot{M} = 10^{-8}$ $M_\odot$ $yr^{-1}$, (b) $\dot{M} = 10^{-7}$ $M_\odot$ $yr^{-1}$. The intensity of each annulus shown is labeled by its radius in units of the stellar radius. Effective temperatures at each annulus can be obtained from Figure 1.

the flux for larger wavelengths is mostly determined by irradiation.

Intensities at each radius do not follow a black body law, characteristic of a single temperature, but at each wavelength the intensity is characteristic of the temperature of the level where $\tau_\lambda = 1$, because of the LTE hypothesis. At wavelengths around strong molecular features, $\tau_\lambda = 1$ occurs high in the atmosphere, where the temperature profile is strongly altered by irradiation. If $T_0/T_{eff} > 1$, the molecular feature is in emission. In the models shown, the bands are in absorption because $T_0/T_{eff} < 1$ at $r \leq 3\ R_*$ (see Figure 1). Similarly, when dust dominates, the shorter the wavelength, the higher in the atmosphere the flux forms, since opacity decreases with wavelength, except around 10 $\mu$m, where the strong opacity in the silicate feature moves $\tau_\lambda = 1$ to outer layers. At large radii, where the opacity is due to dust, this fact produces excess of continuum flux at short wavelengths and emission in the silicate feature around 10 $\mu$m. On the other hand, at long wavelengths where the opacity is lower, the flux is characteristic of the temperature of the deepest atmospheric levels and tends to follow the black body law. For $\lambda > 100$ $\mu$m, the disk becomes optically thin at radii where dust opacity dominates, so that the flux will be determined by its internal structure (D'Alessio *et al.* 1992).

The emergent spectrum of the star and disk system is compared to the flux calculated under the hypothesis that the intensity at each annulus is equal to the Planck function evaluated at the local effective temperature in Figures 4a and 5a. The excess of flux at long wavelengths is apparent. Figures 4a and 5a also show the flux calculated under the hypothesis that the intensity at each annulus is equal to the Planck function evaluated at the reprocessing temperature given by equation (6). This flux is higher than the emergent flux, since the assumptions leading to equation (6) neglect the fact that stellar energy gets deposited in the uppermost atmospheric levels. The difference is larger at long wavelengths, where the flux comes from the outer disk regions where dust opacity dominates. As discussed above, at those radii, the energy deposited in the upper layers gets redistributed in frequency and the spectral energy distribution of each annulus

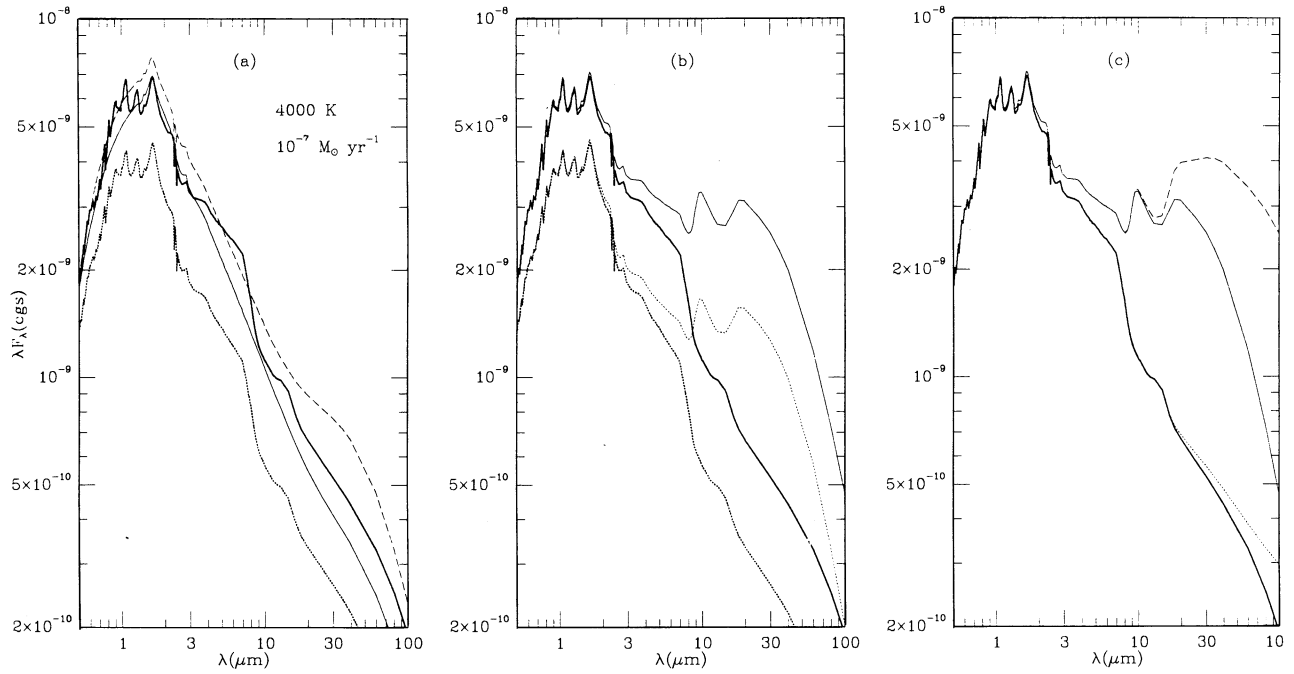


Fig. 4. Emergent flux calculated under different assumptions for a model with $T_* = 4000$ K and $\dot{M} = 10^{-8}$ M$_\odot$ yr$^{-1}$. The heavy continuous line refer to the reference model with $\gamma = 9/8$, and $R_{max} = 1000\ R_*$ at inclination $i = 0°$. (a) Dotted heavy line: $i = 80°$; light continuous line: flux calculated under the assumption that $I_\lambda = B_\lambda[T_{eff}(r)]$, dashed line: flux calculated under the assumption that $I_\lambda = B_\lambda[T_{rep}(r)]$; (b) Dotted heavy line: reference model with $i = 80°$, light continuous line: $\gamma = 5/4$, $i = 0°$, light dotted line: $\gamma = 5/4$, $i = 80°$; (c) light dotted line: $\gamma = 9/8$, and $R_{max} = 8000\ R_*$, light continuous line: $\gamma = 5/4$, $R_{max} = 1000\ R_*$, light dashed line: $\gamma = 5/4$, $R_{max} = 8000\ R_*$, all with $i = 0°$. Fluxes are calculated at 100 pc.

has an excess at short wavelengths, as shown in Figure 3, but this excess is not so apparent in the composite spectrum because it is small compared to the emission of inner radii.

Figures 4b and 5b show the effect of increasing the degree of flaring of the disk for inclinations $i$ = 0° and 80°. The reference model is calculated with $\gamma = 9/8$, and we compare it with a model calculated for $\gamma = 5/4$. As already noted by KH, increasing the flaring of the disk increases the flux, since the area on each disk surface intercepting stellar radiation is larger. The effects are more noticeable for large wavelengths, since at near-infrared wavelengths the emission comes from the inner stellar radii, $\leq 5$ $R_*$ which emit essentially as a flat disk. For this reason, the detailed spectrum in the near-infrared is comparable in both cases, while the emission in the silicate feature increases considerably when the flaring of the disk increases. The increase of flux with $\gamma$ for $\lambda > 10$ $\mu$m is comparable for $\dot{M} = 10^{-8}$ and $10^{-7}$ $M_\odot$ $yr^{-1}$, since irradiation dominates at large radii, as discussed above. The composite spectrum, then, becomes flatter as mass accretion rate increases, although it falls for $\lambda > 30$ $\mu$m.

When the maximum radius of the disk is increased from 13 AU to 100 AU the emergent flux at far-infrared wavelengths increases considerably, as shown in Figures 4c and 5c, while the flux at shorter wavelengths is unchanged. Again, the increase is comparable at the two mass accretion rates considered, despite the differences in the near-infrared, because irradiation dominates at large radii.

### c) *Comparison with Observations*

Table 2 gives magnitudes and colors for models in Table 1. The magnitude $K$ is calculated at 160 pc. Infrared colors $J$ to $M$ have been calculated with filter data from Bessell and Brett (1988). Filters [*8*] and [*11*] refer to the KPNO medium band IR filters with effective wavelength 8.4 and 11.1 $\mu$m and FWHM of 1.7 and 1.72 $\mu$m, respectively (c.f. Rydgren, Strom, and Strom 1972). The filter response has been assumed a gaussian corresponding to this FWHM. IRAS magnitudes have been calculated with filter response in Neugebauer *et al.* (1984). Zero points for other than near-infrared filters have been calculated with a model from Kurucz (1979) corresponding to Vega, with a black-body extrapolation ($T$ = 9400 K) for $\lambda > 2$ $\mu$m . Table 2 also shows the value of infrared indices that have been used in the literature:

$$n = d(log)\lambda F_\lambda)/d(log)\lambda)\,, \qquad (7)$$

which we have calculated from least-squares fitting to fluxes calculated from the broad-band and IRAS filters from 2 to 25 $\mu$m;

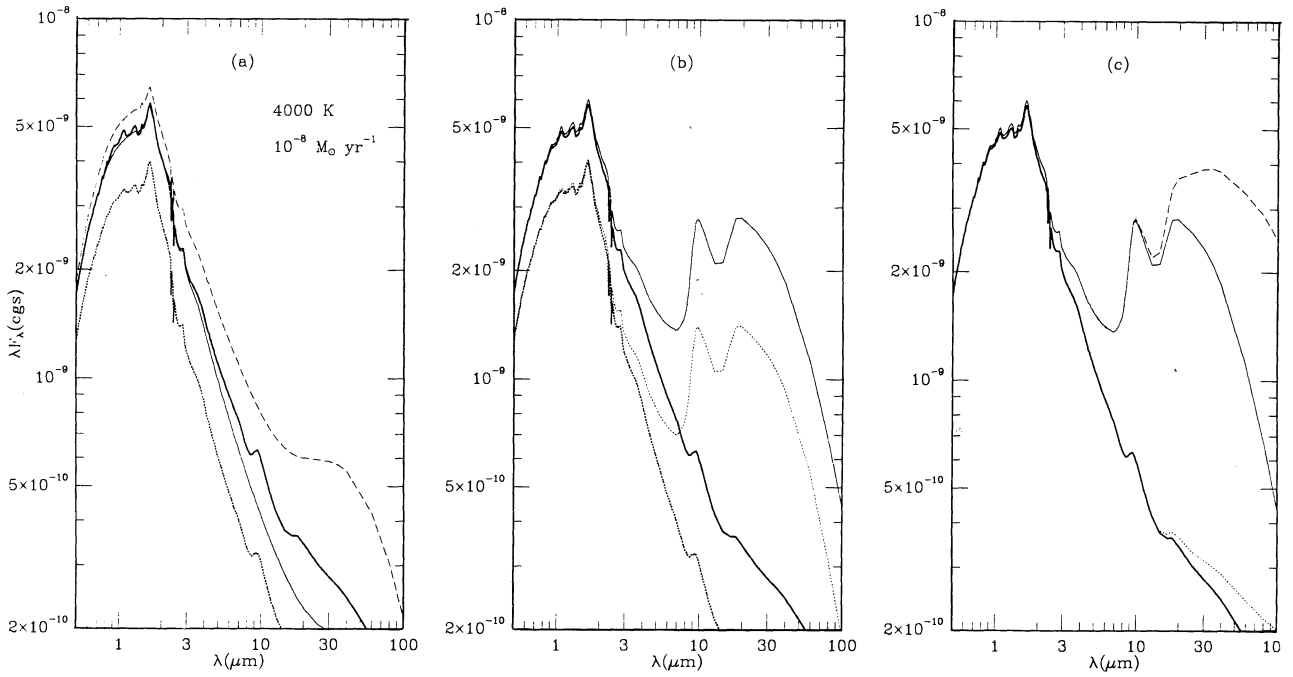


Fig. 5. Same as Figure 4 but for $\dot{M} = 10^{-7}$ $M_\odot$ $yr^{-1}$.

TABLE 2

PREDICTED MAGNITUDES AND COLORS

| Color | $i$(°) | Model Number 1 | 2 | 3 | 4 | 5 | 6 | 7 | 8 | 9 | 10 | 11 | 12 | 13 | 14 | 15 | 16 | 17 | 18 |
|---|---|---|---|---|---|---|---|---|---|---|---|---|---|---|---|---|---|---|---|
| $K$ | 0 | 8.05 | 8.05 | 7.98 | 7.98 | 7.74 | 7.74 | 7.67 | 7.99 | 8.23 | 7.67 | 6.32 | 7.47 | 7.27 | 6.19 | 5.68 | 5.54 | 4.84 | 3.26 |
| | 30 | 8.16 | 8.16 | 8.09 | 8.09 | 7.86 | 7.86 | 7.80 | 8.10 | 8.33 | 7.80 | 6.47 | 7.58 | 7.40 | 6.33 | 5.82 | 5.68 | 4.99 | 3.42 |
| | 60 | 8.53 | 8.53 | 8.47 | 8.47 | 8.28 | 8.28 | 8.22 | 8.48 | 8.66 | 8.22 | 7.02 | 7.99 | 7.83 | 6.87 | 6.33 | 6.20 | 5.54 | 4.00 |
| | 80 | 9.01 | 9.01 | 8.98 | 8.98 | 8.87 | 8.87 | 8.84 | 8.98 | 9.08 | 8.84 | 7.96 | 8.54 | 8.45 | 7.76 | 7.14 | 7.05 | 6.52 | 5.11 |
| $J-K$ | 0 | 1.26 | 1.26 | 1.31 | 1.31 | 1.36 | 1.36 | 1.41 | 1.44 | 1.35 | 1.41 | 1.34 | 1.05 | 1.13 | 1.23 | 1.01 | 1.04 | 1.10 | 1.00 |
| | 30 | 1.25 | 1.25 | 1.29 | 1.29 | 1.35 | 1.35 | 1.39 | 1.42 | 1.33 | 1.39 | 1.33 | 1.03 | 1.10 | 1.21 | 0.98 | 1.02 | 1.08 | 0.99 |
| | 60 | 1.19 | 1.19 | 1.23 | 1.23 | 1.28 | 1.28 | 1.32 | 1.32 | 1.24 | 1.32 | 1.31 | 0.93 | 1.01 | 1.16 | 0.85 | 0.89 | 1.00 | 0.97 |
| | 80 | 1.09 | 1.09 | 1.11 | 1.11 | 1.15 | 1.15 | 1.17 | 1.15 | 1.11 | 1.17 | 1.24 | 0.76 | 0.81 | 1.01 | 0.54 | 0.59 | 0.77 | 0.91 |
| $H-K$ | 0 | 0.36 | 0.36 | 0.40 | 0.40 | 0.50 | 0.50 | 0.53 | 0.50 | 0.40 | 0.53 | 0.59 | 0.37 | 0.45 | 0.54 | 0.54 | 0.54 | 0.49 | 0.40 |
| | 30 | 0.35 | 0.35 | 0.39 | 0.39 | 0.48 | 0.48 | 0.51 | 0.48 | 0.38 | 0.51 | 0.60 | 0.36 | 0.44 | 0.54 | 0.53 | 0.54 | 0.49 | 0.41 |
| | 60 | 0.30 | 0.30 | 0.33 | 0.33 | 0.41 | 0.41 | 0.45 | 0.40 | 0.31 | 0.44 | 0.59 | 0.31 | 0.38 | 0.53 | 0.48 | 0.50 | 0.48 | 0.42 |
| | 80 | 0.20 | 0.20 | 0.22 | 0.22 | 0.28 | 0.28 | 0.30 | 0.26 | 0.21 | 0.30 | 0.49 | 0.20 | 0.25 | 0.42 | 0.32 | 0.34 | 0.39 | 0.39 |
| $K-L$ | 0 | 0.62 | 0.62 | 0.74 | 0.74 | 0.96 | 0.96 | 1.02 | 1.13 | 1.16 | 1.02 | 1.13 | 0.69 | 0.88 | 1.08 | 0.88 | 0.93 | 0.95 | 0.89 |
| | 30 | 0.60 | 0.60 | 0.72 | 0.72 | 0.94 | 0.94 | 1.00 | 1.10 | 1.12 | 1.00 | 1.13 | 0.67 | 0.86 | 1.07 | 0.88 | 0.92 | 0.95 | 0.89 |
| | 60 | 0.52 | 0.52 | 0.63 | 0.63 | 0.84 | 0.84 | 0.91 | 0.97 | 0.97 | 0.91 | 1.10 | 0.60 | 0.78 | 1.04 | 0.83 | 0.88 | 0.93 | 0.88 |
| | 80 | 0.33 | 0.33 | 0.41 | 0.41 | 0.59 | 0.59 | 0.65 | 0.65 | 0.61 | 0.65 | 0.98 | 0.42 | 0.57 | 0.90 | 0.67 | 0.73 | 0.83 | 0.86 |
| $K-M$ | 0 | −0.02 | −0.02 | 0.24 | 0.24 | 0.57 | 0.57 | 0.68 | 0.88 | 0.99 | 0.68 | 0.82 | −0.01 | 0.37 | 0.73 | 0.25 | 0.35 | 0.50 | 0.48 |
| | 30 | −0.06 | −0.06 | 0.21 | 0.20 | 0.54 | 0.54 | 0.66 | 0.84 | 0.94 | 0.65 | 0.81 | −0.03 | 0.35 | 0.72 | 0.24 | 0.34 | 0.50 | 0.48 |
| | 60 | −0.18 | −0.18 | 0.07 | 0.06 | 0.41 | 0.41 | 0.53 | 0.66 | 0.72 | 0.52 | 0.77 | −0.14 | 0.23 | 0.67 | 0.17 | 0.28 | 0.46 | 0.47 |
| | 80 | −0.48 | −0.48 | −0.29 | −0.29 | 0.03 | 0.03 | 0.15 | 0.20 | 0.19 | 0.15 | 0.60 | −0.44 | −0.10 | 0.47 | −0.05 | 0.07 | 0.33 | 0.44 |
| $K-12$ | 0 | 1.60 | 1.60 | 3.13 | 3.17 | 2.11 | 2.11 | 3.09 | 3.38 | 3.60 | 3.11 | 2.24 | 1.73 | 2.00 | 2.18 | 2.61 | 2.55 | 2.33 | 2.01 |
| | 30 | 1.55 | 1.55 | 3.09 | 3.13 | 2.08 | 2.08 | 3.05 | 3.33 | 3.54 | 3.08 | 2.23 | 1.69 | 1.97 | 2.17 | 2.59 | 2.54 | 2.32 | 2.01 |
| | 60 | 1.35 | 1.35 | 2.88 | 2.92 | 1.91 | 1.91 | 2.89 | 3.12 | 3.29 | 2.91 | 2.18 | 1.52 | 1.82 | 2.11 | 2.50 | 2.46 | 2.28 | 2.00 |
| | 80 | 0.78 | 0.78 | 2.27 | 2.30 | 1.40 | 1.40 | 2.37 | 2.50 | 2.58 | 2.40 | 1.99 | 1.00 | 1.34 | 1.88 | 2.18 | 2.18 | 2.11 | 1.96 |
| $K-25$ | 0 | 3.52 | 3.60 | 5.73 | 6.11 | 3.92 | 3.97 | 5.53 | 5.84 | 6.08 | 5.88 | 3.97 | 3.70 | 3.89 | 3.96 | 4.53 | 4.45 | 4.12 | 3.57 |
| | 30 | 3.47 | 3.56 | 5.68 | 6.06 | 3.89 | 3.93 | 5.50 | 5.80 | 6.02 | 5.85 | 3.96 | 3.66 | 3.86 | 3.95 | 4.51 | 4.43 | 4.12 | 3.57 |
| | 60 | 3.25 | 3.33 | 5.47 | 5.85 | 3.71 | 3.76 | 5.33 | 5.58 | 5.76 | 5.68 | 3.91 | 3.47 | 3.70 | 3.88 | 4.43 | 4.36 | 4.08 | 3.55 |
| | 80 | 2.60 | 2.68 | 4.83 | 5.21 | 3.16 | 3.20 | 4.80 | 4.94 | 5.03 | 5.15 | 3.71 | 2.89 | 3.18 | 3.64 | 4.10 | 4.06 | 3.90 | 3.51 |
| $K-60$ | 0 | 5.92 | 6.18 | 7.83 | 8.93 | 6.21 | 6.39 | 7.60 | 7.91 | 8.15 | 8.65 | 6.03 | 6.01 | 6.14 | 6.00 | 6.25 | 6.17 | 5.80 | 5.03 |
| | 30 | 5.86 | 6.12 | 7.77 | 8.88 | 6.16 | 6.33 | 7.56 | 7.86 | 8.09 | 8.62 | 5.99 | 5.97 | 6.09 | 5.96 | 6.22 | 6.14 | 5.77 | 5.00 |
| | 60 | 5.61 | 5.88 | 7.54 | 8.65 | 5.94 | 6.12 | 7.37 | 7.62 | 7.80 | 8.44 | 5.88 | 5.76 | 5.90 | 5.84 | 6.11 | 6.03 | 5.68 | 4.90 |
| | 80 | 4.94 | 5.21 | 6.90 | 8.02 | 5.37 | 5.56 | 6.83 | 6.97 | 7.07 | 7.90 | 5.65 | 5.16 | 5.36 | 5.57 | 5.77 | 5.72 | 5.48 | 4.83 |
| $[8]-[11]$ | 0 | 0.68 | 0.69 | 1.24 | 1.27 | 0.53 | 0.53 | 1.03 | 1.05 | 1.07 | 1.05 | 0.43 | 0.76 | 0.62 | 0.47 | 1.00 | 0.92 | 0.71 | 0.50 |
| | 30 | 0.68 | 0.68 | 1.24 | 1.27 | 0.53 | 0.53 | 1.03 | 1.05 | 1.07 | 1.05 | 0.43 | 0.76 | 0.62 | 0.47 | 0.99 | 0.92 | 0.71 | 0.50 |
| | 60 | 0.66 | 0.67 | 1.23 | 1.26 | 0.52 | 0.52 | 1.02 | 1.05 | 1.07 | 1.05 | 0.43 | 0.75 | 0.62 | 0.47 | 0.99 | 0.92 | 0.72 | 0.50 |
| | 80 | 0.60 | 0.60 | 1.19 | 1.22 | 0.50 | 0.50 | 1.00 | 1.02 | 1.04 | 1.02 | 0.43 | 0.69 | 0.59 | 0.46 | 0.98 | 0.91 | 0.71 | 0.49 |
| $\alpha_{12}$[a] | 0 | 0.66 | 0.55 | −0.18 | −0.62 | 0.80 | 0.74 | 0.00 | −0.02 | −0.04 | −0.40 | 0.90 | 0.60 | 0.70 | 0.85 | 0.66 | 0.69 | 0.82 | 1.12 |
| | 30 | 0.67 | 0.56 | −0.18 | −0.62 | 0.80 | 0.75 | 0.00 | −0.02 | −0.04 | −0.40 | 0.90 | 0.60 | 0.70 | 0.85 | 0.66 | 0.69 | 0.82 | 1.12 |
| | 60 | 0.69 | 0.59 | −0.17 | −0.61 | 0.82 | 0.76 | 0.01 | −0.01 | −0.03 | −0.40 | 0.90 | 0.62 | 0.71 | 0.85 | 0.66 | 0.70 | 0.82 | 1.13 |
| | 80 | 0.80 | 0.69 | −0.15 | −0.58 | 0.87 | 0.81 | 0.03 | 0.01 | −0.01 | −0.38 | 0.91 | 0.69 | 0.76 | 0.87 | 0.67 | 0.71 | 0.83 | 1.13 |
| $\alpha_{25}$[b] | 0 | 0.60 | 0.41 | 0.92 | 0.16 | 0.71 | 0.58 | 0.94 | 0.94 | 0.94 | 0.21 | 0.96 | 0.69 | 0.76 | 0.97 | 1.31 | 1.31 | 1.36 | 1.58 |
| | 30 | 0.61 | 0.42 | 0.92 | 0.16 | 0.73 | 0.59 | 0.96 | 0.95 | 0.95 | 0.21 | 0.99 | 0.70 | 0.77 | 1.00 | 1.33 | 1.33 | 1.38 | 1.62 |
| | 60 | 0.63 | 0.43 | 0.94 | 0.17 | 0.77 | 0.63 | 0.98 | 0.98 | 0.97 | 0.22 | 1.05 | 0.72 | 0.81 | 1.06 | 1.35 | 1.36 | 1.44 | 1.70 |
| | 80 | 0.65 | 0.46 | 0.95 | 0.17 | 0.80 | 0.65 | 0.99 | 0.98 | 0.98 | 0.22 | 1.08 | 0.73 | 0.83 | 1.08 | 1.36 | 1.37 | 1.46 | 1.74 |
| $n$[c] | 0 | −0.93 | −0.90 | −0.02 | 0.11 | −0.81 | −0.80 | −0.16 | −0.05 | 0.05 | −0.05 | −0.82 | −0.86 | −0.81 | −0.82 | −0.51 | −0.56 | −0.71 | −0.93 |
| | 30 | −0.95 | −0.92 | −0.03 | 0.09 | −0.82 | −0.81 | −0.17 | −0.06 | 0.03 | −0.06 | −0.82 | −0.87 | −0.82 | −0.82 | −0.51 | −0.56 | −0.71 | −0.93 |
| | 60 | −1.03 | −1.00 | −0.11 | 0.02 | −0.88 | −0.87 | −0.23 | −0.13 | −0.05 | −0.11 | −0.84 | −0.94 | −0.88 | −0.84 | −0.54 | −0.59 | −0.73 | −0.93 |
| | 80 | −1.27 | −1.24 | −0.35 | −0.23 | −1.07 | −1.06 | −0.42 | −0.35 | −0.30 | −0.30 | −0.91 | −1.16 | −1.06 | −0.92 | −0.66 | −0.69 | −0.78 | −0.94 |

a. $\alpha_{12} = \log(\lambda_{12}F_{12}/\lambda_{25}F_{25})/\log(\lambda_{25}/\lambda_{12})$; b. $\alpha_{25} = \log(\lambda_{25}F_{25}/\lambda_{60}F_{60})/\log(\lambda_{60}/\lambda_{25})$; c. $n = d(\log\lambda F_\lambda)/d(\log\lambda)$.

$$\alpha_{12} = log(\lambda_{12}F_{12}/\lambda_{25}F_{25})/log(\lambda_{25}/\lambda_{12}), \quad (8)$$

and

$$\alpha_{25} = log(\lambda_{25}F_{25}/\lambda_{60}F_{60})/log(\lambda_{60}/\lambda_{25}), \quad (9)$$

(Weintraub 1990).

Figures 6a and 6b compare theoretical near-infrared colors from Table 2 with colors for TTS in Rydgren *et al.* (1984). Observed colors have been dereddened with $A_V$ from Cohen and Kuhi (1979). Theoretical colors have uncertainties of roughly 0.1 magnitudes, estimated from comparison between colors calculated for the theoretical photospheres and colors for stars of type K7V and K2V in

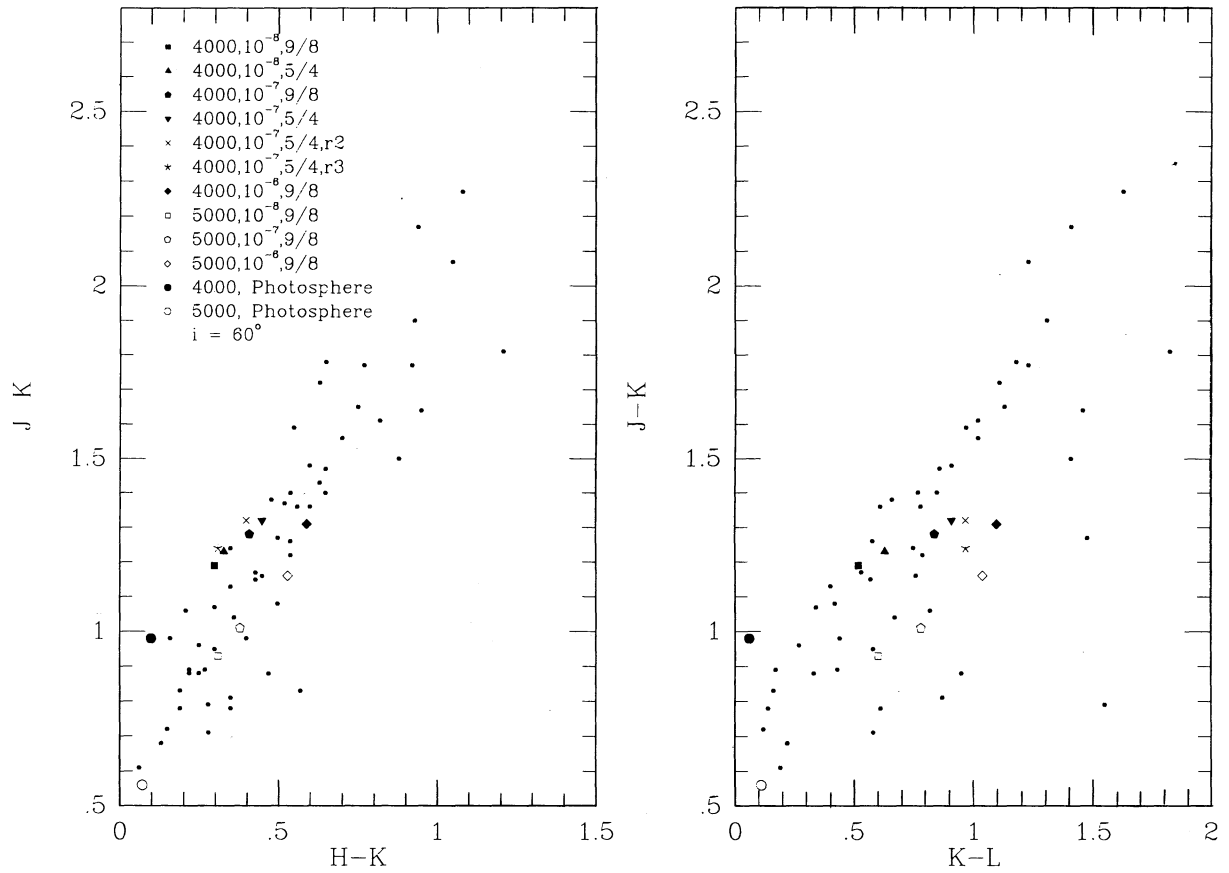


Fig. 6. (a) Comparison between predicted and observed near-infrared colors *J–K* versus *H–K* for T Tauri stars. Observations are from Rydgren *et al.* (1984) and are shown with filled dots. Observations have been corrected for reddening with $A_V$ from Cohen and Kuhi (1979) and the standard reddening law. Model parameters are specified in the figure, where each model is labeled by the values of the stellar effective temperature, the mass accretion rate, and the flaring of the disk $\gamma$. Models identified with "r2" (cross) and "r3" (star) correspond to models with inner holes of radius 2 $R_*$ and 3 $R_*$, respectively. Predictions are shown for $i = 60°$. (b) Comparison between predicted and observed near-infrared colors *J–K* versus *K–L* for T Tauri stars. Symbols as in Figure 6a.

Johnson (1966). Theoretical colors are shown for an inclination of 60°, which corresponds to the most likely viewing angle for a random distribution of orientations. The effect of increasing inclination is to make the colors bluer, because the photospheric contribution becomes more important.

Irradiated optically thick accretion disks can explain near-infrared colors for roughly 40% of the stars. Approximately 30% of the stars in this sample have colors between the photosphere and the bluest star-disk colors. This could be understood in terms of optically thin disks, although detailed models have yet to be built for this case. Alternatively, a physical hole could also explain the effect. We have calculated models with central holes of size 2 $R_*$ and 3 $R_*$, identified in Figure 6a with "r2" and "r3", respectively. These holes make *J – K* bluer, because the photospheric contribution becomes more conspicuous when the emission of the inner disk regions is absent.

A fraction of ~ 30% of the stars have infrared colors redder than the reddest model colors. We have tried several possibilities to make the colors redder. Increasing the mass accretion rate can make redder colors, because the cooler inner disk regions contribute more light than the stellar photosphere (see Figure 2a). However, this increase in color cannot explain the reddest observed colors. Increasing the degree of disk flaring also increases the infrared colors, but again not sufficiently. Hence, although roughly 70% of the stellar colors could be explained in terms of irradiated optically thin or thick accretion disk, or disks with central holes; the near-infrared colors of 30% of the stars cannot be understood with conventional models of accretion disks.

In Figure 7, we compare observed values of $\alpha_{12}$ and $\alpha_{25}$, defined in equations (8) and (9), taken from Weintraub (1990) with predicted colors. Symbols are the same as in Figure 6a and again theoretical colors are shown at $i = 60°$. Continuous lines in the figure join models calculated with $R_{max}$ = 1000, $R_* \sim$ 13 AU and $R_{max}$ = 8000, $R_* \sim$ 100 AU, with colors $\alpha$ decreasing for increasing $R_{max}$. The effect of increasing the degree of flaring is to make the $\alpha$ colors more negative, since the flux at large wavelengths increases. However, the flux at wavelengths > 60 $\mu$m does not increase as much as the flux at shorter wavelengths, because at those wavelengths the flux begins to drop for lack of emitting material in the outer regions. Increasing the maximum radius of the disk shifts the flux cut-off to larger wavelengths, and both $\alpha_{12}$ and $\alpha_{25}$ become more negative, although the change is much larger in $\alpha_{25}$.

The comparison shown in Figure 7 indicates that most of the observed far-infrared colors in TTS can be understood in terms of irradiated accretion disks with different degrees of flaring and different sizes. Around 20% of the stars in the sample have $\alpha$ colors which cannot be understood in terms of the effects described. Since for most of them the flux excess is at large wavelengths ($\alpha_{25}$ more negative), it could be argued that an infalling envelope could be contributing at those wavelengths (Adams, Lada, and Shu 1987; Barsony and Kenyon 1991).

As discussed above, the 10 $\mu$m silicate feature is a conspicuous feature in the spectrum, indicative of mass accretion rate and of the degree of flaring.

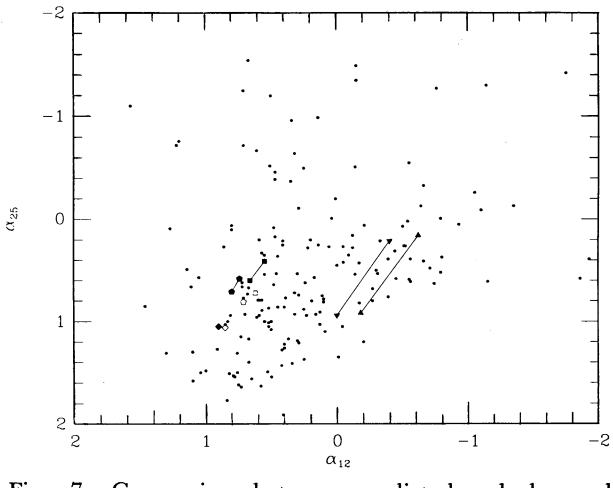


Fig. 7. Comparison between predicted and observed IRAS indices $\alpha_{12}$ and $\alpha_{25}$, defined in equations (8) and (9), for T Tauri stars. Observed values (filled dots) are from Weintraub (1990). Symbols as in Figure 6a. Continuous lines joint models calculated with $R_{max}$ = 1000 $R_* \sim$ 13 AU and $R_{max}$ = 8000, $R_* \sim$ 100 AU, with colors $\alpha$ decreasing for increasing $R_{max}$.

To use this feature for obtaining disk parameters, however, spectrophotometric data is required to determine if it is in absorption or in emission, but little information is available. Cohen and Witteborn (1985) have published spectrophotometry at 10 $\mu$m for a small number of TTS and Herbig Ae/Be stars. In some cases, the data are too noisy or the continuum in the short-wavelength side is not discernible; but in other cases the feature can be seen either in absorption or in emission. Rydgren, Strom, and Strom (1972) give medium band colors at 8 and 11 $\mu$m for a larger number of TTS and Herbig's Ae/Be stars. The magnitude at 11.1 $\mu$m, which has a width of 1.72 $\mu$m includes the silicate feature. The magnitude at 8.4 $\mu$m is more representative of the continuum next to the feature, although it also includes some of it (FWHM = 1.7 $\mu$m). The color [*8*]-[*11*] represents then in a very crude way the strength of the silicate feature relative to the continuum at shorter wavelengths. We have decided to combine the two sets of data to attempt a comparison between predictions and observations.

In Figure 8 we compare model predictions for the [*8*]-[*11*] color with observations from Rydgren, Strom, and Strom (1972). We show schematically the regions where emission or absorption in the silicate feature is expected, and indicate with different symbols the stars for which either emission or ab-

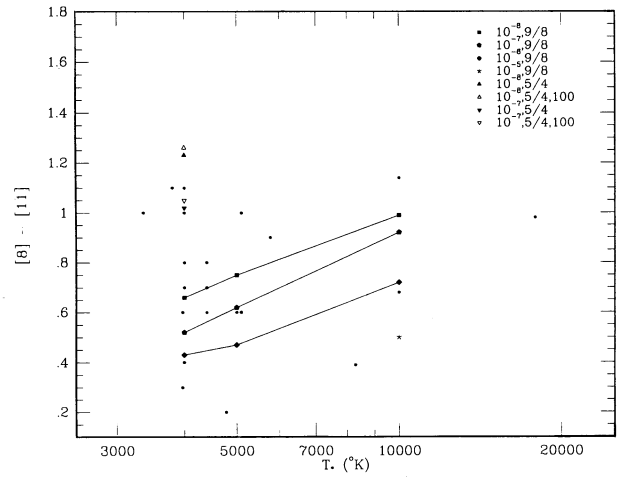


Fig. 8. Comparison between predicted and observed *[8]-[11]* color for stars of different effective temperature $T_*$. The *[8]-[11]* color is a measure of the silicate feature strength (see text). Model parameters other than the stellar temperature are specified in the figure, where each model is labeled by the values of the the mass accretion rate, $\gamma$, and $R_{max}$ in units of AU. When $R_{max}$ is not given, it is taken as $R_{max}$ = 13 AU. Observations are from Rydgren, Strom, and Strom (1972), marked differently according to Cohen and Witteborn (1985) data: filled circles, emission; open circles, absorption; x's, no information.

sorption is present in Cohen and Witteborn (1985) observations. In general, spectrophotometric data, when available, corroborate the theoretical expectations. The two stars that show the silicate feature in absorption but have a [*8*]-[*11*] color consistent with silicate emission are DG Tau and DR Tau. These stars are highly variable, and it is possible that the disk structure varied significantly over the $\approx 10$ year period between the two sets of observations. The models seem to explain the observations fairly well. Even though most of the TTS in the plot could be explained in terms of irradiated disks with low degree of flaring, those with large [*8*]-[*11*] could be understood only with more flared disks. The degree of flaring is then highly variable among TTS. The few Ae/Be for which data is available indicate that the average $\dot{M}$ for them is higher than in TTS (a conclusion also reached from the study of the excess infrared luminosity by Strom *et al.* [1990]) and that the degree of flaring is also variable among them.

## IV. DISCUSSION

We have carried out calculations for the emergent flux of irradiated, optically thick accretion disks with different degrees of flaring, and various values for the maximum radii and size of central holes. These models can explain near-infrared colors for $\sim$ 40% of TTS, although there seems to be systematic deficit of flux at L, which cannot be accounted for by uncertainties in the theoretical models (see Figures 6a and 6b). 30% of the stars, with colors intermediate between the photosphere and the calculated disk models could in principle be explained by disks with optically thin regions, although detailed models have yet to be constructed. The other 30% of the stars with very red near-infrared colors cannot be explained by the models. The excess implies that the temperature structure in the inner disks of these stars is very different from that in the standard disks we have assumed.

In this study, we have taken as parameters of the problem the stellar effective temperature, the mass accretion rate, the flaring of the disk, and its maximum radius. For the class of TTS, which we have investigated in more detail, the far-infrared colors are very dependent on the last two parameters. Stars with large excess can be explained by a large degree of flaring and a large disk size, still within the limits estimated from [O I] observations (Edwards *et al.* 1987); the excess can be so large that index $n$ given in Table 2 can get to be greater than zero. Around 20% of the stars have far-infrared excesses too large to be accounted for by these models, and maybe they can be explained in terms of emission in infalling envelopes, since the flux excess is larger at $\lambda \sim 60$ $\mu$m. The near-infrared colors, on the other hand, are not very sensitive to the flaring of the disk and to its maximum radius, basically because the emission comes from the inner radii, which are essentially flat if the height of the disk follows a power law with radius as assumed in these calculations. An alternative then, as mentioned above, is that the temperature structure is different from that of a standard disk as calculated here. It is possible that a treatment in which the inner disk structure is solved subject to the condition of irradiation giving the height of the disk self-consistently, would give better agreement between theory and observations. Alternatively, other factors may be altering the inner disk structure from that expected for a standard steady accretion disk. If the star had a magnetosphere that disrupted the disk at some radius (Calvet and Hartmann 1991), then the material would fall onto the star mostly along field lines, and the region in the disk where the magnetosphere joins the disk would be highly perturbed. Also, if there were infalling material at small radii, then irradiation on this material would change the near-infrared colors (Kenyon and Hartmann 1991).

One important result of this work and Paper I is that there are spectral features that can be used as indicators of disk parameters: CO, TiO, and $H_2O$ molecular bands, and the silicate feature. The last three, specially the silicate, are disk features with little or no contamination from the photosphere, in contrast to the near-infrared bands of CO. The results of §III indicate that the strength in absorption of the $H_2O$ and the TiO bands depends mostly on the mass accretion rate for known $T_*$, without being affected by other disk parameters. Once $\dot{M}$ is known, the flaring of the disk, measured by $\gamma$, could be obtained from the appearance (emission or absorption) and strength of the silicate feature. Alternatively, the spectral slope between $\approx 3$ $\mu$m and $\approx 20$ $\mu$m could be used to estimate the amount of flaring, and the silicate feature could give $\dot{M}$. The maximum radius of the disk can then be known from the flux beyond $\sim 10$ $\mu$m. This approach, however, requires high resolution spectrophotometry in the infrared, which is not available at the present. With the present data, we have at least determined that predictions for the silicate feature strength are consistent with observations. Theoretical predictions can be arranged in diagrams as that in Figure 8 so that comparison with observations can give system parameters. However, this task should wait until better data become available.

## V. SUMMARY

We have calculated the emergent flux for systems composed of a young star and a steady, physically

thin, flared, optically thick accretion disk subject to irradiation from the central star. Energy emerges at each radius from the disk atmosphere, in which the temperature structure is determined by irradiation and by the (constant) viscous flux coming from the interior of the disk. We have found the following:

(1) The emergent continuum flux is lower than that calculated assuming that all the stellar energy is deposited at the bottom of the atmosphere at each annulus of the disk. Some energy is absorbed in the upper layers, redistributed in frequency, and emitted at wavelengths where it is hidden by the emission from inner annuli. Thus, disks must have either larger flaring or higher mass accretion rates than previously thought.

(2) If in a given annulus in the disk, irradiation is more important than viscous heating, there is a temperature inversion in the atmosphere and strong spectral features appear in emission. Alternatively, strong features are in absorption if viscous heating is more important. Therefore, these features appear in absorption in the spectrum of the whole disk if there is a large zone where viscous heating dominates. Since, for a given stellar temperature, the disk radius where heating due to irradiation becomes more important than viscous heating increases with mass accretion rate, the strength of CO, $H_2O$, TiO absorption bands, and of the silicate feature then measures the mass accretion rate.

(3) Disk flaring affects the spectrum of TTS mostly for $\lambda > 3$ $\mu$m, because features at shorter wavelengths form in the inner regions, $r < 5$ $R_*$, that behave essentially as a flat disk. The maximum radius of the disk, considered to be between $\sim 10$ and 100 AU, determines the spectrum for $\lambda > 10$ $\mu$m, because of the low temperatures of the emitting regions.

(4) Optically thick accretion disks can reproduce $\sim 40\%$ of the near-infrared color observations of TTS. Inner holes in the disk make systems bluer, because the system tends to have the near-infrared colors of the photosphere. This suggests that disks with inner holes (or optically thin) may explain 30% of the objects with colors intermediate between the photosphere and the bluest near-infrared colors predicted with optically thick disks. Roughly 30% of the objects in the sample considered have near-infrared colors too red to be accounted for by the models.

(5) Large degrees of flaring and large disk sizes, $R_{max} \leq 100$ AU (consistent with the [O I] observations), can explain objects with large far-infrared excess in TTS. Objects with very large excess at $\lambda \geq 60$ $\mu$m, 20% of the stars in the sample considered, could be explained by either a larger size for the disk or an infalling envelope as an additional component of the system (Adams, Lada, and Shu 1987; Barsony and Kenyon 1991).

(6) The observed silicate feature strength, in emission or in absorption, as measured by the [*8*]-[*11*] color can be explained consistently by the theoretical models. This feature is sensitive to $\dot{M}$ and very sensitive to the flaring of the disk. The observed strength of the feature indicates that the degree of flaring is highly variable among TTS.

(7) Disk parameters could be estimated with the following observables: $\dot{M}$ could be determined from the strength in absorption of the molecular bands of $H_2O$, CO, and TiO; the flaring of the disk could be determined from the appearance (emission or absorption) and strength of the silicate feature, once $\dot{M}$ is known; alternatively, the spectral slope between $\approx 3$ $\mu$m and $\approx 20$ $\mu$m could be used to estimate the amount of flaring, and the silicate feature could give $\dot{M}$; the maximum radius of the disk could be determined from the flux at $\lambda > 10$ $\mu$m, if $\dot{M}$ and the degree of flaring were known. High resolution infrared spectrophotometric data are required to test these predictions.

We thank L. Hartmann for instructive comments and suggestions. We thank S. Kenyon for useful suggestions and for his careful proofreading of the manuscript. G.M.C. has been partially supported by a fellowship from Fundación Gran Mariscal de Ayacucho. P.D. has been supported by UNAM (DGAPA) Grant No. 100589. Part of this work has been supported by Project No. C-380-89 of the CDCH of the Universidad de Los Andes and by the International Exchange Program of the Smithsonian Institution.

## REFERENCES

Adams, F.C., Lada, C.L., & Shu, F.H. 1987, ApJ, 312, 788
Alexander, D.R., Augason, G.C., & Johnson, H.R. 1989, ApJ, 345, 1014
Alexander, D.R., Johnson, H.R., & Rypma, R.L. 1983, ApJ, 272, 773
Auman Jr., J. 1967, ApJS, 14, 171
Barsony, M., & Kenyon, S.J. 1991, ApJ, submitted
Bertout, C., Basri, G.S., & Bouvier, J. 1988, ApJ, 330, 350
Bessell, M.S., & Brett, J.M. 1988, PASP, 100, 1134
Calvet, N., & Hartmann, L. 1992, ApJ, in press
Calvet, N., Patiño, A., Magris C., G., & D'Alessio, P. 1991, ApJ, 380, 617, Paper I
Carbon, D.F., & Gingerich, O. 1969, in Theory and Observations of Normal Stellar Atmospheres, ed. O. Gingerich, (Cambridge: MIT Press), p. 377
Clarke, C.J., Lin, D.N.C., & Pringle, J.E. 1990, MNRAS, 242, 439
Cohen, M., & Kuhi, L.V. 1979, ApJS, 36, 359
Cohen, M., & Witteborn, F.C. 1985, ApJ, 294, 345
Collins, J.G., & Fay, T.D. Jr. 1974, J. Quant. Spectrosc. Rad. Transf., 14, 1259
D'Alessio, P., Cantó, J., Lizano, S., Calvet, N., & Raga, A.C. 1992, in preparation.

Davis, S.P., Littleton, J.E., & Phillips, J.G. 1986, ApJ, 309, 449
Draine, B.T. 1987, Princeton Obs. Preprint No. 213
Draine, B.T., & Lee, H.M. 1984, ApJ, 285, 89
Edwards, S., Cabrit, S., Strom, S.E., Heyer, I., & Strom, K.M. 1987, ApJ, 321, 473
Hartmann, L., & Kenyon, S.J. 1985, ApJ, 299, 859
Johnson, H.L. 1966, ARA&A, 4, 193
Kenyon, S.J., & Hartmann, L. 1987, ApJ, 323, 714
____. 1991, ApJ, in press
Kirby-Docken, K., & Liu, B. 1978, ApJS, 36, 359
Kurucz, R. 1979, ApJS, 40, 1
Ludwig, C.B., Malkmus, W., Reardon, J.E., & Thompson, J.A.L. 1973, Handbook of Infrared Radiation from Combustion Gasses, (NASA SP-3080)
Mantz, A.W., Maillard, J.-P., Roh, W.B., & Rao, K.N. 1975, J. Molec. Spectrosc., 57, 155
Milne, E.A. 1930, Handbuch der Astrophysik, 3, 65
Nuegebauer, G. *et al.* 1984, Science, 224, 14
Rydgren, A.E., Strom, S.E., & Strom, K.M. 1972, ApJS, 30, 307
Rydgren, A.E., Schmelz, J.T., Zak, D.S., & Vrba, F.J. 1984, Pub.US Naval Obs., Vol. XXV, Part I
Strittmatter, P.A. 1974, A&A, 32, 7
Shakura, N.I., & Sunyaev, R.A. 1973, A&A, 24, 337
Tsuji, T. 1966, Pub.Astr.Soc.Japan, 18, 127
Strom, S.E., Keene, J., Edwards, S., Hillenbrand, Strom, K., Gauvin, L., & Condon, G. 1990, in Angular Momentum Evolution of Young Stars, ed. J.R. Stauffer, (Dordrecht: Kluwer Academic Publishers), in press
Weintraub, D.A. 1990, ApJS, 74, 575

Nuria Calvet, Gladis Magris, Alberto Patiño: Centro de Investigaciones de Astronomía, Apartado Postal 264, Mérida 5101-A, Venezuela.
Paola D'Alessio: Instituto de Astronomía, UNAM, Apartado Postal 70-264, 04510 México D. F., México.